

# Universality of shear-banding instability and crystallization in sheared granular fluid

MEHEBOOB ALAM<sup>1</sup>†, PRIYANKA SHUKLA<sup>1</sup>  
AND STEFAN LUDING<sup>2</sup>

<sup>1</sup>Engineering Mechanics Unit, Jawaharlal Nehru Center for Advanced Scientific Research  
Jakkur PO Bangalore 560064, India

<sup>2</sup>MultiScale Mechanics, Faculty of Science and Technology, University of Twente, PO Box 217,  
7500 AE Enschede, The Netherlands

(Received 19 April 2008 and in revised form 1 August 2008)

The linear stability analysis of an uniform shear flow of granular materials is revisited using several cases of a Navier–Stokes-level constitutive model in which we incorporate the global equation of states for pressure and thermal conductivity (which are accurate up to the maximum packing density  $\nu_m$ ) and the shear viscosity is allowed to diverge at a density  $\nu_\mu$  ( $< \nu_m$ ), with all other transport coefficients diverging at  $\nu_m$ . It is shown that the emergence of shear-banding instabilities (for perturbations having no variation along the streamwise direction), that lead to shear-band formation along the gradient direction, depends crucially on the choice of the constitutive model. In the framework of a dense constitutive model that incorporates only collisional transport mechanism, it is shown that an accurate global equation of state for pressure or a viscosity divergence at a lower density or a stronger viscosity divergence (with other transport coefficients being given by respective Enskog values that diverge at  $\nu_m$ ) can induce shear-banding instabilities, even though the original dense Enskog model is stable to such shear-banding instabilities. For any constitutive model, the onset of this shear-banding instability is tied to a universal criterion in terms of constitutive relations for viscosity and pressure, and the sheared granular flow evolves toward a state of lower ‘dynamic’ friction, leading to the shear-induced band formation, as it cannot sustain increasing dynamic friction with increasing density to stay in the homogeneous state. A similar criterion of a lower viscosity or a lower viscous-dissipation is responsible for the shear-banding state in many complex fluids.

---

## 1. Introduction

One challenge in granular flow research is to devise appropriate hydrodynamic/continuum models to describe its macroscopic behaviour. Rapid granular flows (Campbell 1990; Goldhirsch 2003) can be modelled well by an idealized system of smooth hard spheres with inelastic collisions. The kinetic theory of dense gases has been modified to obtain Navier–Stokes-like (NS) hydrodynamic equations, with an additional equation for the fluctuation kinetic energy of particles (i.e. granular energy) that incorporates the dissipative nature of particle collisions. Such NS-order hydrodynamic models have been widely used as prototype models to gain insight into the ‘microscopic’ understanding of various physical phenomena involved in granular flows.

† Email address for correspondence: meheboob@jncasr.ac.in

The plane Couette flow has served as a prototype model problem to study the rheology (Lun *et al.* 1984; Jenkins & Richman 1985; Campbell 1990; Sela & Goldhirsch 1998; Alam & Luding 2003*a,b*, 2005; Tsai, Voth & Gollub 2003; Gayen & Alam 2008) and dynamics (Hopkins & Louge 1991; McNamara 1993; Tan & Goldhirsch 1997; Alam & Nott 1997, 1998; Conway & Glasser 2004; Alam *et al.* 2005; Alam 2005, 2006; Gayen & Alam 2006; Saitoh & Hayakawa 2007) of granular materials. In the rapid shear flow, the linear stability analyses of plane Couette flow (Alam & Nott 1998; Alam 2006) showed that this flow admits different types of stationary and travelling-wave instabilities, leading to pattern formation. One such instability is the ‘shear-banding’ instability in which the homogeneous shear flow breaks into alternating dense and dilute regions of particles along the gradient direction. This is dubbed ‘shear-banding’ instability since the ‘nonlinear’ saturation of this instability (Alam & Nott 1998; Alam *et al.* 2005; Shukla & Alam 2008) leads to alternate layers of dense and dilute particle bands in which the shear rate is high/low in dilute/dense regions, respectively, leading to ‘shear localization’ (Varnik *et al.* 2003). This is reminiscent of shear-band formation in shear-cell experiments (Savage & Sayed 1984; Losert *et al.* 2000; Mueth *et al.* 2000; Alam & Luding 2003*b*; Tsai *et al.* 2003): when a dense granular material is sheared the shearing is confined within a few particle layers (i.e. a shear band) and the rest of the material remains unsheared, leading to the two-phase flows of dense and dilute regions. Alam & Nott (1998) and Alam *et al.* (2005) showed that the kinetic-theory-based hydrodynamic models are able to predict the co-existence of dilute and dense regimes of such shear-banding patterns.

The above problem has been reanalysed (Khain & Meerson 2006), with reference to shear-band formation, with a constitutive model which is likely to be valid in the dense limit. These authors showed that their ‘dense’ constitutive model does not admit the shear-banding instabilities of Alam & Nott (1998); however, a single modification so that the shear viscosity diverges at a density lower than other transport coefficients resulted in the appearance of two-phase-type solutions of dilute and dense flows that are reminiscent of shear-banding instabilities. That the viscosity diverges stronger/faster than other transport coefficients has also been incorporated previously in a constitutive model by Losert *et al.* (2000) that yields a satisfactory prediction for shear bands in an experimental Couette flow in three dimensions.

We revisit this problem to understand the influence of different Navier–Stokes-order constitutive models (as detailed in §2) on the shear-banding instabilities in granular plane Couette flow. More specifically, we will pinpoint how the effects of various models, some of them involving the global equation of state and the viscosity divergence (at a density lower than the maximum packing), change the shear-banding instabilities predicted by Alam & Nott (1998). For the sake of a systematic overview, we will also discuss the instability results based on special limiting cases of these models. One important finding is that a global equation of state (without viscosity divergence at a lower density) leads to a shear-banding instability in the framework of ‘dense’ model that incorporates only the collisional transport mechanism. Even with the local equation of state, if we use a constitutive relation for viscosity that has a stronger divergence (at the same maximum packing density) than other transport coefficients, we recover shear-banding instabilities in the framework of the dense-model of Haff (1983). This brings us to a crossroad: are there any connections among the results of Alam & Nott, Khain & Meerson, and the present work? Is there any universal criterion for the onset of the shear-banding instability in granular shear flow? Such a universality for the shear-banding instability indeed exists, solely in

terms of the constitutive relations, as we show in this paper. Possible connections of the present criterion of a lower dynamic friction for the shear-banding state to explain the onset of shear-banding in many complex fluids as well as in an elastic hard-sphere fluid are discussed.

## 2. Balance equations and constitutive model

We use a Navier–Stokes-level hydrodynamic model for which we need balance equations for mass, momentum and granular temperature:

$$\left(\frac{\partial}{\partial t} + \mathbf{u} \cdot \nabla\right) \varrho = -\varrho \nabla \cdot \mathbf{u}, \quad (2.1)$$

$$\varrho \left(\frac{\partial}{\partial t} + \mathbf{u} \cdot \nabla\right) \mathbf{u} = -\nabla \cdot \mathbf{P}, \quad (2.2)$$

$$\frac{\text{dim}}{2} \varrho \left(\frac{\partial}{\partial t} + \mathbf{u} \cdot \nabla\right) T = -\nabla \cdot \mathbf{q} - \mathbf{P} : \nabla \mathbf{u} - \mathcal{D}. \quad (2.3)$$

Here  $\varrho = mn = \rho_p v$  is the mass density,  $m$  the particle mass,  $n$  the number density,  $\rho_p$  the material density and  $v$  the area/volume fraction of particles;  $\mathbf{u}$  is the coarse-grained velocity field and  $T$  is the granular temperature of the fluid. Note that the granular temperature,  $T = \langle C^2 / \text{dim} \rangle$ , is defined as the mean-square fluctuation velocity, with  $\mathbf{C} = (\mathbf{c} - \mathbf{u})$  being the peculiar velocity of particles and  $\mathbf{c}$  the instantaneous particle velocity;  $\text{dim}$  is the dimensionality of the system and hereinafter we focus on the two-dimensional ( $\text{dim} = 2$ ) system of an inelastic ‘hard-disk’ fluid. The flux terms are the stress tensor,  $\mathbf{P}$ , and the granular heat flux,  $\mathbf{q}$ ;  $\mathcal{D}$  is the rate of dissipation of granular energy per unit volume – for these three terms we need appropriate constitutive relations which are detailed below.

### 2.1. General form of Newtonian constitutive model: model A

The standard Newtonian form of the stress tensor and the Fourier law of heat flux are:

$$\mathbf{P} = (p - \zeta \nabla \cdot \mathbf{u}) \mathbf{I} - 2\mu \mathbf{S}, \quad (2.4)$$

$$\mathbf{q} = -\kappa \nabla T, \quad (2.5)$$

where  $\mathbf{I}$  is the identity tensor and  $\mathbf{S}$  the deviator of the deformation rate tensor. Here  $p$ ,  $\mu$ ,  $\zeta$  and  $\kappa$  are the pressure, shear viscosity, bulk viscosity and thermal conductivity of the granular fluid, respectively.

Focusing on the nearly elastic limit ( $e \rightarrow 1$ ) of an inelastic hard-disk (of diameter  $d$ ) fluid, the constitutive expressions for  $p$ ,  $\mu$ ,  $\zeta$ ,  $\kappa$  and  $\mathcal{D}$  are given by

$$\left. \begin{aligned} p(v, T) &= \rho_p f_1(v) T, & \mu(v, T) &= \rho_p d f_2(v) \sqrt{T}, \\ \zeta(v, T) &= \rho_p d f_3(v) \sqrt{T}, & \kappa(v, T) &= \rho_p d f_4(v) \sqrt{T}, \\ \mathcal{D}(v, T) &= \frac{\rho_p}{d} f_5(v, e) T^{3/2}, \end{aligned} \right\} \quad (2.6)$$

where  $f_1$ – $f_5$  are non-dimensional functions of the particle area fraction  $v$  (Gass 1971; Jenkins & Richman 1985):

$$f_1(v) = v + 2v^2 \chi, \quad (2.7)$$

$$f_2(v) = \frac{\sqrt{\pi}}{8\chi} + \frac{\sqrt{\pi}}{4}v + \frac{\sqrt{\pi}}{8} \left(1 + \frac{8}{\pi}\right) v^2\chi, \quad (2.8)$$

$$f_3(v) = \frac{2}{\sqrt{\pi}}v^2\chi, \quad (2.9)$$

$$f_4(v) = \frac{\sqrt{\pi}}{2\chi} + \frac{3\sqrt{\pi}}{2}v + \sqrt{\pi} \left(\frac{2}{\pi} + \frac{9}{8}\right) v^2\chi, \quad (2.10)$$

$$f_5(v, e) = \frac{4}{\sqrt{\pi}}(1 - e^2)v^2\chi. \quad (2.11)$$

These constitutive expressions give good predictions for transport coefficients of nearly elastic granular fluid upto a density of  $v \approx 0.55$  (see figure 2 of Alam & Luding 2003a). In the above expressions,  $\chi(v)$  is the contact radial distribution function which is taken to be of the following form (Henderson 1975)

$$\chi(v) = \frac{1 - 7v/16}{(1 - v/v_m)^2}, \quad (2.12)$$

that diverges at some finite density  $v = v_m$ . For the ideal case of point particles (i.e. in one dimension, Torquato 1995), we have  $v_m = 1$  which is unrealistic for macroscopic grains at very high densities; there are two other choices for this diverging density: the random close packing density  $v_r = v_m = 0.82$  or the maximum packing density  $v_m = \pi/2\sqrt{3} \approx 0.906$  in two-dimensions (Torquato 1995); upto some moderate density ( $v \sim 0.5$ ), there is no difference in the value of  $\chi(v)$  for any choice of  $v_m = 1$  or 0.906 or 0.82. The range of validity of different variants of model radial distribution functions is discussed in an forthcoming paper (Luding 2008).

We shall denote the above constitutive model (2.6)–(2.11), with the contact radial distribution function being given by (2.12), as ‘model A’. Since the stability results do not differ qualitatively with either choice of the numerical value for  $v_m$  ( $=0.82$  or 0.906 or 1), we will present all results with  $v_m = \pi/2\sqrt{3}$  in (2.12) (except in figure 12d, see §5.2).

Now we consider the dilute and dense limits of model A. It should be noted that each transport coefficient has contributions from the ‘kinetic’ and ‘collisional’ modes of transport: while the former is dominant in the Boltzmann limit ( $v \rightarrow 0$ ), the latter is dominant in the dense limit ( $v \rightarrow v_m$ ). For example, the pressure can be decomposed into its kinetic and collisional contributions:

$$p = p^k + p^c = \rho_p(f_1^k + f_1^c)T. \quad (2.13)$$

To obtain the constitutive expressions for the dilute and dense regimes, we must take the appropriate limit of all functions  $f_1$ – $f_4$ :

$$\left. \begin{aligned} f_1 &= f_1^k + f_1^c, & f_2 &= f_2^k + f_2^c, \\ f_3 &= f_3^k + f_3^c, & f_4 &= f_4^k + f_4^c. \end{aligned} \right\} \quad (2.14)$$

Based on this decomposition, we have the following two limiting cases of model A.

2.1.1. Dilute limit: model  $A_0$ 

For this dilute ( $\nu \rightarrow 0$ ) model,  $\chi(\nu) \rightarrow 1$  and the constitutive expressions are assumed to contain contributions only from the kinetic mode of transport:

$$\left. \begin{aligned} f_1 &\equiv f_1^k(\nu) = \nu, & f_2 &\equiv f_2^k(\nu) = \frac{\sqrt{\pi}}{8} + \frac{\sqrt{\pi}}{4}\nu, \\ f_3 &\equiv f_3^k(\nu) = 0, & f_4 &\equiv f_4^k(\nu) = \frac{\sqrt{\pi}}{2} + \frac{3\sqrt{\pi}}{2}\nu, \\ f_5 &\equiv f_5(\nu \rightarrow 0) = \frac{4}{\sqrt{\pi}}(1 - e^2)\nu^2. \end{aligned} \right\} \quad (2.15)$$

We shall call this ‘model  $A_0$ ’. Note that  $f_5$  has only the leading-order collisional contribution, since no energy is dissipated in kinetic (free-flow) motion.

 2.1.2. Dense limit: model  $A_d$ 

For this dense model, the constitutive expressions are assumed to contain contributions only from collisional mode of transport:

$$\left. \begin{aligned} f_1 &\equiv f_1^c(\nu) = 2\nu^2\chi, & f_2 &\equiv f_2^c(\nu) = \frac{\sqrt{\pi}}{8}\left(1 + \frac{8}{\pi}\right)\nu^2\chi, \\ f_3 &\equiv f_3^c(\nu) = \frac{2}{\sqrt{\pi}}\nu^2\chi, & f_4 &\equiv f_4^c(\nu) = \sqrt{\pi}\left(\frac{2}{\pi} + \frac{9}{8}\right)\nu^2\chi, \\ f_5 &\equiv f_5(\nu, e) = \frac{4}{\sqrt{\pi}}(1 - e^2)\nu^2\chi. \end{aligned} \right\} \quad (2.16)$$

We shall call this ‘model  $A_d$ ’ which is merely Haff’s model (1983).

 2.2. Model  $B$ : global equation of state (EOS)

In two-dimensions, a global equation of state for pressure has been proposed by Luding (2001):

$$p/\rho_p T \equiv f_1(\nu) = \nu + \nu(P_4 + m(\nu)[P_{dense} - P_4]), \quad \forall \quad 0 \leq \nu \leq \nu_m = \frac{\pi}{2\sqrt{3}}, \quad (2.17)$$

where

$$\left. \begin{aligned} P_4 &= 2\nu\chi_4, \\ \chi_4(\nu) &= \frac{1 - 7\nu/16}{(1 - \nu)^2} - \frac{\nu^3}{128(1 - \nu)^4}, \\ P_{dense} &= \frac{2\nu_m h_3(\nu_m - \nu)}{(\nu_m - \nu)} - 1, \\ h_3(\nu_m - \nu) &= 1 - 0.04(\nu_m - \nu) + 3.25(\nu_m - \nu)^3, \\ m(\nu) &= [1 + \exp(-(\nu - \nu_f)/m_0)]^{-1}. \end{aligned} \right\} \quad (2.18)$$

Here  $\nu_f$  is the freezing point density, and  $m(\nu)$  is a merging function that selects  $P_4$  for  $\nu \ll \nu_f$  and  $P_{dense}$  for  $\nu \gg \nu_f$ ; the value of  $m_0$  is taken to be 0.012 along with a freezing density of  $\nu_f = 0.7$ . It should be noted that the above functional form of  $f_1(\nu)$ , (2.17), is a monotonically increasing function of  $\nu$ , and it has been verified (Luding 2001, 2002; Garcia-Rojo, Luding & Brey 2006) from molecular dynamics simulations of elastic hard-disk systems that the numerical values for different constants in (2.18) are accurate (within much less than 1% except around  $\nu_f$ ) upto the maximum packing density.

Rewriting (2.17) as

$$f_1(v) = v + 2v^2\chi^p(v), \quad (2.19)$$

we can define an ‘effective’ contact radial distribution function for pressure:

$$\begin{aligned} \chi^p(v) &= \frac{1}{2v} (P_4 + m(v) [P_{dense} - P_4]) \\ &= \chi_4 + m(v) \left[ \frac{h_3(v_m - v)}{v(1 - v/v_m)} - \frac{1}{2v} - \chi_4 \right] \quad \text{with} \quad v_m = \frac{\pi}{2\sqrt{3}}. \end{aligned} \quad (2.20)$$

It should be noted here that this functional form of  $\chi^p(v)$  has been verified by molecular dynamics simulations of plane shear flow of frictional inelastic disks (Volfson, Tsimring & Aranson 2003). In particular, they found that the simulation data on  $G(v) = v\chi^p(v)$  agree with the predictions of (2.20); however, its divergence appears to occur at the random close packing limit in two dimensions ( $v_m = v_r = 0.82$ ).

Similar to pressure, a global equation for thermal conductivity has been suggested by Garcia-Rojo *et al.* (2006) which is also accurate upto the maximum packing density. More specifically, the non-dimensional function of density for thermal conductivity (equation (2.10)) is replaced by

$$f_4(v) = \frac{\sqrt{\pi}}{2\chi^k(v)} + \frac{3\sqrt{\pi}}{2}v + \sqrt{\pi} \left( \frac{2}{\pi} + \frac{9}{8} \right) v^2\chi^k(v), \quad (2.21)$$

where  $\chi^k(v)$  is the ‘effective’ contact radial distribution function for thermal conductivity:

$$\chi^k(v) = \chi(v, v_m = 1) + m(v) \left[ \frac{h_3(v_m - v)}{v(1 - v/v_m)} - \frac{1}{2v} - \chi(v, v_m = 1) \right], \quad (2.22)$$

with  $\chi(v, v_m = 1)$  being obtained from (2.12) by putting  $v_m = 1$ .

The model A with the above global equation of state for pressure and the global equation for thermal conductivity is called ‘model B’. Note that the dilute limit of model B is the same as that of model A; however, the dense limits of both models are different in the choice of the equation of state and thermal conductivity.

Now we identify two subsets of model B: ‘model B<sup>p</sup>’ and ‘model B<sup>k</sup>’ where the former is model B with a global equation of state for pressure (2.17) only and the latter is model B with a global equation for thermal conductivity (2.21) only. As clarified in the previous paragraph, the remaining transport coefficients of model B are same as in model A.

### 2.3. Model C: viscosity divergence

Here we consider a variant of model A which incorporates another ingredient in the constitutive model: the shear viscosity diverges at a density lower than other transport coefficients (Garcia-Rojo *et al.* 2006). This can be incorporated in the corresponding dimensionless function for the shear viscosity (2.8):

$$f_2^\mu(v) = f_2(v) \left( 1 + \frac{0.037}{v_\mu - v} \right), \quad (2.23)$$

which diverges at a density,  $v = v_\mu < v_m$ , that is lower than the close packing density. The first term on the right-hand-side is the standard Enskog term, (2.8), and the second term incorporates a correction due to the viscosity divergence. For all results shown here, we use  $v_\mu = 0.71$  which was observed for the unsheared case (Garcia-Rojo *et al.* 2006); note, however, that the precise density at which viscosity diverges in a shear flow can be larger than 0.71 (see figure 6 of Alam & Luding 2003b).

The model with all transport coefficients as in model A but with its viscosity divergence being at a lower density is termed ‘model C’. Similar to model A, we can recover the dilute and dense limits of model C, by separating the kinetic and collisional contributions to each transport coefficient. The dense limit of model C is, however, reached at  $\nu = \nu_\mu$  owing to the viscosity divergence.

#### 2.4. Model D: global equation of state and viscosity divergence

This is the most general model in which we incorporate: (i) the global equation of state for pressure (2.17); (ii) the global equation for thermal conductivity (2.21); and (iii) the viscosity divergence (2.23). The other transport coefficients of model D are same as in model A.

### 3. Plane shear and linear stability

Let us consider the plane shear flow of granular materials between two walls that are separated by a distance  $\tilde{H}$ : the top wall is moving to the right with a velocity  $U_w/2$  and the bottom wall is moving to the left with the same velocity. We impose no-slip and zero heat-flux boundary conditions at both walls:

$$\mathbf{u} = \pm U_w/2, \quad \mathbf{q} = 0 \quad \text{at} \quad y = \pm \tilde{H}/2. \quad (3.1)$$

The equations of motion for the steady and fully developed shear flow admit the following solution:

$$\mathbf{u} = [u(y), v(y)] = [(U_w/\tilde{H})y, 0], \quad v(y) = \text{const} = \bar{v}, \quad T = d^2 \left( \frac{du}{dy} \right)^2 \frac{f_2(v)}{f_5(v)}. \quad (3.2)$$

The shear rate,  $du/dy = U_w/\tilde{H}$ , is uniform (constant) across the Couette gap, and this solution will hereinafter be called the *uniform shear solution*. Note that if viscosity diverges at  $\nu = \nu_\mu$ , there is no uniform shear solution for  $\nu > \nu_\mu$ , i.e. the uniform shear flow is possible only for densities  $0 < \nu < \nu_\mu$ .

We have non-dimensionalized all quantities by using  $\tilde{H}$ ,  $\tilde{H}/U_w$  and  $U_w$  as the reference length, time and velocity scales, respectively. The explicit forms of dimensionless balance equations as well as the dimensionless transport coefficients are given in Appendix A. There are three dimensionless control parameters to characterize our problem: the scaled Couette gap  $H = \tilde{H}/d$ , the mean density (area fraction)  $\nu = \bar{\nu}$  and the restitution coefficient  $e$ . Hereinafter all quantities are expressed in dimensionless form.

#### 3.1. Linear stability

The stability analysis of the plane shear flow has been thoroughly investigated (Alam & Nott 1998; Alam 2005, 2006; Alam *et al.* 2005) using the constitutive models of class A for which all transport coefficients diverge at the maximum packing fraction  $\nu \rightarrow \nu_m$ , as outlined in §2.1. The same analysis is carried out here for a specific type of perturbations that are invariant along the streamwise/flow ( $x$ ) direction, having variations along the gradient ( $y$ ) direction only. This implies that the  $x$ -derivatives of all quantities are set to zero ( $\partial/\partial x(\cdot) = 0$ ) in the governing equations. See Alam & Nott (1998) for mathematical details of the analysis.

Consider the stability of the uniform shear solution (3.2) against perturbations that have spatial variations along the  $y$ -direction only, e.g. the density field can be written as  $\nu(y, t) = \nu + \nu'(y, t)$ , with the assumption of small-amplitude perturbations,  $|\nu'(y, t)/\nu| \ll 1$ , for the linear analysis. Linearizing around the uniform shear solution,

we obtain a set of partial differential equations:

$$\frac{\partial X}{\partial t} = \mathcal{L}X \quad \text{with} \quad \mathcal{B}X \equiv \left(1, 1, \frac{d}{dy}\right) (u', v', T') = 0, \tag{3.3}$$

where  $X = (v', u', v', T')$  is the vector of perturbation fields,  $\mathcal{L}$  is the linear stability operator and  $\mathcal{B}$  denotes the boundary operator (i.e. zero slip, zero penetration and zero heat flux). Assuming exponential solutions in time  $X(y, t) = \hat{X}(y) \exp(\omega t)$ , we obtain a differential-eigenvalue problem:

$$\omega \hat{X} = \mathcal{L} \left( \frac{d^2}{dy^2}, \frac{d}{dy}, \dots \right) \hat{X} \quad \text{with} \quad \mathcal{B}\hat{X} = 0, \tag{3.4}$$

where  $\hat{X}(y) = (\hat{v}, \hat{u}, \hat{v}, \hat{T})(y)$  is the unknown disturbance vector that depends on  $y$ . Here,  $\omega = \omega_r + i\omega_i$  is the complex frequency whose real part  $\omega_r$  denotes the growth/decay rate of perturbations and the imaginary part  $\omega_i$  is its frequency which characterizes the propagating ( $\omega_i \neq 0$ ) or stationary ( $\omega_i = 0$ ) nature of the disturbance. The flow is stable or unstable if  $\omega_r < 0$  or  $\omega_r > 0$ , respectively.

3.2. *Analytical solution: dispersion relation and its roots*

Before presenting numerical stability results (§4), we recall that the above set of ordinary differential equations (3.4) admits an analytical solution (Alam & Nott 1998):

$$(\hat{v}(y), \hat{T}(y)) = (v_1, T_1) \cos k_n(y \pm 1/2), \tag{3.5}$$

$$(\hat{u}(y), \hat{v}(y)) = (u_1, v_1) \sin k_n(y \pm 1/2), \tag{3.6}$$

where  $k_n = n\pi$  is the ‘discrete’ wavenumber along  $y$ , with  $n = 1, 2, \dots$  being the mode number that tells us the number of zero-crossing of the density/temperature eigenfunctions along  $y \in (-1/2, 1/2)$ . With this, (3.4) boils down to an algebraic eigenvalue problem:

$$\mathcal{A}X_1 = \omega X_1, \tag{3.7}$$

where  $X_1 = (v_1, u_1, v_1, T_1)$  and  $\mathcal{A}$  is a  $4 \times 4$  matrix. This leads to a fourth-order dispersion relation in  $\omega$ :

$$\omega^4 + a_3\omega^3 + a_2\omega^2 + a_1\omega + a_0 = 0, \tag{3.8}$$

with coefficients

$$\left. \begin{aligned} a_0 &= \frac{1}{H^4}a_{04} + \frac{1}{H^6}a_{06}, & a_1 &= \frac{1}{H^2}a_{12} + \frac{1}{H^4}a_{14} + \frac{1}{H^6}a_{16}, \\ a_2 &= \frac{1}{H^2}a_{22} + \frac{1}{H^4}a_{24}, & a_3 &= a_{30} + \frac{1}{H^2}a_{32}. \end{aligned} \right\} \tag{3.9}$$

Here, the terms  $a_{ij}$  are real functions of density ( $v$ ), temperature ( $T$ ), and the restitution coefficient ( $e$ ) whose explicit forms are given in Appendix B.

Out of four roots of (3.8), two roots are real and the other two form a complex-conjugate pair. It is possible to obtain an approximate analytical solution for these four roots using the standard asymptotic expansion for large Couette gaps ( $H \equiv \tilde{H}/d$ ), with the corresponding small parameter being  $H^{-1}$ . The real roots have the approximations for large  $H$ :

$$\omega^{(1)} = -\frac{1}{H^2} \left( \frac{a_{04}}{a_{12}} \right) + O(H^{-4}), \tag{3.10}$$



$$\omega^{(2)} = \omega_0^{(2)} + \frac{1}{H^2} \frac{[a_{12} + a_{22}\omega_0^{(2)} + a_{32}\omega_0^{(2)2}]}{\omega_0^{(2)}(3a_{30} + 4\omega_0^{(2)})} + O(H^{-4}), \tag{3.11}$$

where

$$\omega_0^{(2)} = -\frac{1}{\nu} f_5 T^{1/2} < 0. \tag{3.12}$$

The real and imaginary parts of the conjugate pair,

$$\omega^{(3,4)} = \omega_r^{(3,4)} \pm i \omega_i^{(3,4)}, \tag{3.13}$$

have the asymptotic approximations for large  $H$ :

$$\omega_r^{(3,4)} = \frac{1}{H^2} \left[ \frac{a_{04} + (a_{12}^2/a_{30}^2) - (a_{12}a_{22}/a_{30})}{2a_{12}} \right] + O(H^{-4}), \tag{3.14}$$

$$(\omega_i^{(3,4)})^2 = \frac{1}{H^2} \left( \frac{a_{12}}{a_{30}} \right) + O(H^{-4}). \tag{3.15}$$

For full models (i.e.  $A$ ,  $B$ ,  $C$  and  $D$ ), it can be verified that  $\omega_r^{(3,4)}$  is always negative, making the first real root  $\omega^{(1)}$ , given by (3.10), the least-stable mode. However, for the dense models (i.e.  $A_d$ ,  $B_d$ ,  $C_d$  and  $D_d$ ),  $\omega_r^{(3,4)}$  could be positive, making the travelling waves, given by (3.13), the least-stable mode at low densities. These predictions have been verified against numerical values obtained from spectral method as discussed in §4.

#### 4. Stability results: comparison among different models

For results in this section, the differential eigenvalue problem (3.4) has been discretized using the Chebyshev spectral method (Alam & Nott 1998) and the resultant algebraic eigenvalue problem has been solved using the QR-algorithm of the Matlab software. The degree of the Chebyshev polynomial was set to 20 which was found to yield accurate eigenvalues. In principle, we could solve (3.8) to obtain eigenvalues, but it provides eigenvalues only for a given mode number  $n = 1, 2, \dots$  in one shot; therefore, we must solve (3.8) for several  $n$  to determine the growth rate of the most unstable mode. The advantage of the numerical solution of (3.4) is that it provides all leading eigenvalues in one shot.

##### 4.1. Results for model $A$ and its dilute and dense limits

As mentioned before, the stability analysis of the uniform shear flow with a three-dimensional variant (i.e. for spheres) of model  $A$  has been performed previously (Alam & Nott 1998; Alam 2005, 2006; Alam *et al.* 2005). Even though the results for our two-dimensional model are similar to those for the three-dimensional model, we show a few representative results for this constitutive model for the sake of a complete, systematic study and for comparison with other models; note that the results for model  $A_0$  and model  $A_d$  are new.

The phase diagram, separating the zones of stability and instability, in the  $(\nu, H)$ -plane is shown in figure 1 for model  $A$ . The flow is unstable inside the neutral contour, denoted by '0', and stable outside; a few positive growth-rate contours are also displayed. For the same parameter set, from the respective contours of the frequency,  $\omega_i$ , in the  $(\nu, H)$ -plane it has been verified that these instabilities are stationary, i.e.  $\omega_i = 0$ . It is seen that there is a minimum value of the Couette gap

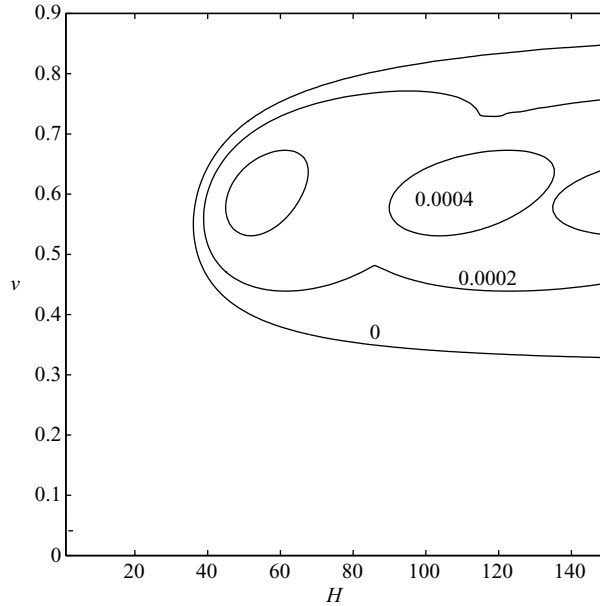


FIGURE 1. Phase diagram, showing the positive growth-rate contours, for model A:  $e=0.9$ ,  $\nu_m = \pi/2\sqrt{3}$ . The flow is unstable inside the neutral contour, denoted by '0', and stable outside.

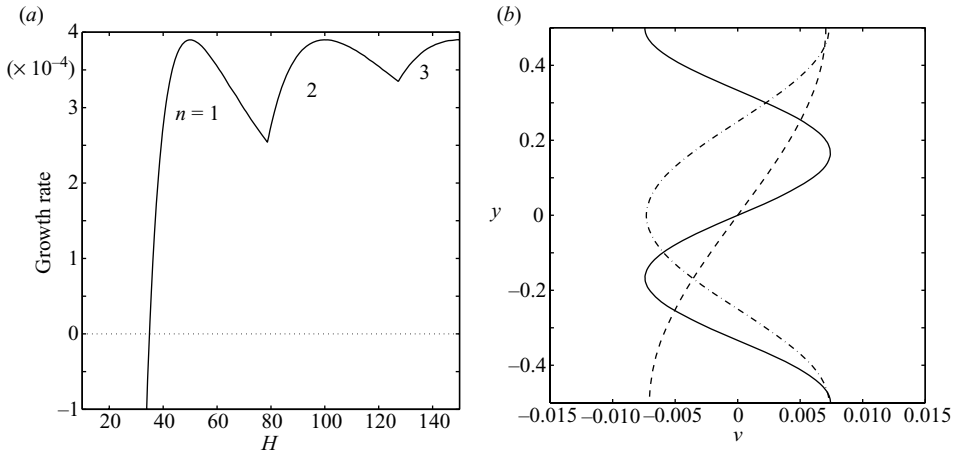


FIGURE 2. (a) Variation of the growth rate of the least stable mode with  $H$  for  $\nu=0.5$  and  $e=0.9$ . (b) Density eigenfunctions,  $\hat{v}(y)$ , of the least stable mode at ---,  $H=50$ ; -·-, 100; —, 150.

( $H = H_{cr}$ ) and a minimum density ( $\nu = \nu_{cr}$ ) below which the flow remains stable. With increasing value of  $e$ , the neutral contour shifts towards the right, i.e.  $H_{cr}$  increases and hence the flow becomes more stable with increasing  $e$ . We shall discuss the dependence of  $e$  on the shear-banding instability and the related instability length scale in § 5.2.

Figure 2(a) shows the variation of the growth rate of the least stable mode,  $\omega_r^l = \max \omega_r$ , with Couette gap for  $\nu=0.5$ , with other parameters as in figure 1. The kinks on the growth-rate curve correspond to crossing of modes  $n=1, 2, 3, \dots$ . This can be verified from figure 2(b) which displays density eigenfunctions for three

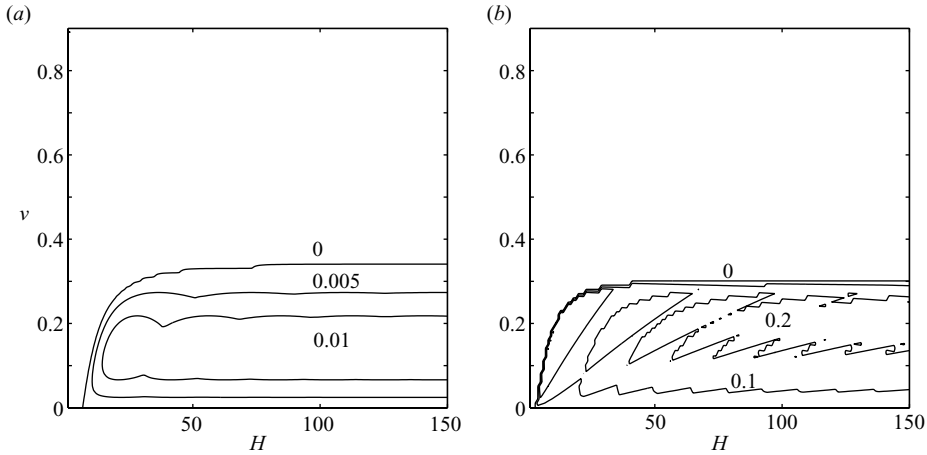


FIGURE 3. (a) Phase diagram, showing the positive growth-rate contours, for model  $A_d$  (i.e. the dense limit of model A):  $e=0.9$ ,  $v_m = \pi/2\sqrt{3}$ . (b) Contours of frequency, indicating that the instability in (a) is due to travelling waves.

values of Couette gaps  $H = 50, 100$  and  $150$ . The density eigenfunction at  $H = 50$  corresponds to the mode  $n = 1$  (i.e.  $\hat{v} \sim \cos(\pi(y \pm 1/2)) = \sin(\pi y)$ , see (3.5)), the other two at  $H = 100, 150$  correspond to modes  $n = 2, 3$  (i.e.  $\hat{v} \sim \cos(2\pi y)$  and  $\sin(3\pi y)$ , respectively). In fact, there is an infinite hierarchy of such modes as  $H \rightarrow \infty$  which has been discussed before (Alam & Nott 1998; Alam *et al.* 2005).

For the dilute limit of model A (i.e. model  $A_0$ ), there are stationary instabilities at finite densities ( $v > 0$ ), and the stability diagram (not shown for brevity) in the  $(H, v)$ -plane looks similar to that for model A (figure 1), but the range of  $H$  over which the flow is unstable is much larger. As expected, both model A and model  $A_0$  predict that the flow is stable in the Boltzmann limit ( $v \rightarrow 0$ ).

Figure 3(a) shows the analogue of figure 1 for model  $A_d$  for which the constitutive relations are expected to be valid in the dense limit (since the constitutive relations contain the collisional part only, §2.1.2); figure 3(b) shows the contours of frequency (corresponding to the least-stable mode) in the  $(H, v)$ -plane. The flow is unstable to travelling-wave instabilities inside the neutral contour. For this dense model, the crossings of different instability modes ( $n = 1, 2, \dots$ ) with increasing Couette gap  $H$  and their frequency variations can be ascertained from figure 4. From a comparison between figures 1 and 3, the following differences are noted:

- (i) Model  $A_d$  predicts that the flow is stable in the dense limit which is in contrast to the prediction of the full model (i.e. model A) for which the dense flow is unstable. This is a surprising result since the kinetic contribution to transport coefficients is small in the dense limit, and hence both model A and model  $A_d$  are expected to yield similar results.
- (ii) There is a travelling-wave (TW) instability at low densities ( $v < 0.3$ ) for model  $A_d$  which is absent in model A. Since model  $A_d$  is devoid of the kinetic modes of momentum transfer and hence not applicable at low densities, we call the TW-modes in figure 3(a) ‘anomalous’ modes and they vanish when both kinetic and collisional effects are incorporated as in the full model A.

One conclusion that can be drawn from the results of three variants of model A is that the choice of the constitutive model is crucial for the prediction of shear-banding instability. We shall return to this point in §5.

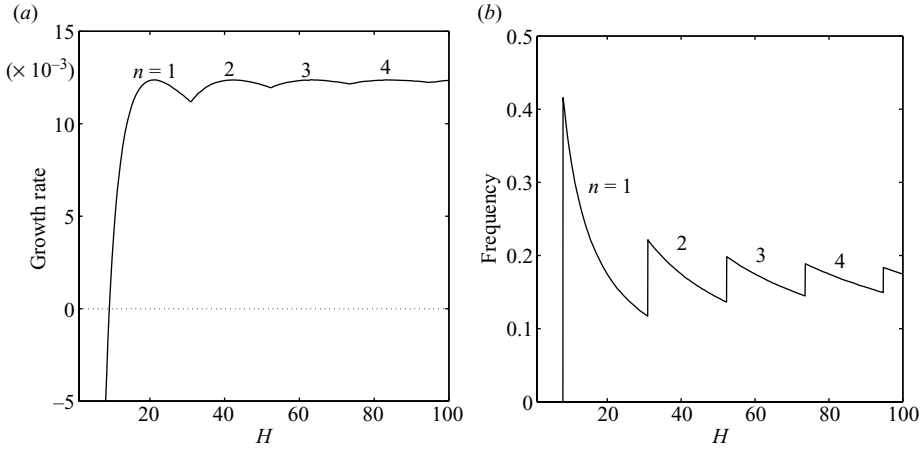


FIGURE 4. Variations of (a) the growth rate and (b) the frequency of the least stable mode with  $H$  for  $\nu = 0.1$  and  $e = 0.9$ . Other parameters as in figure 3.

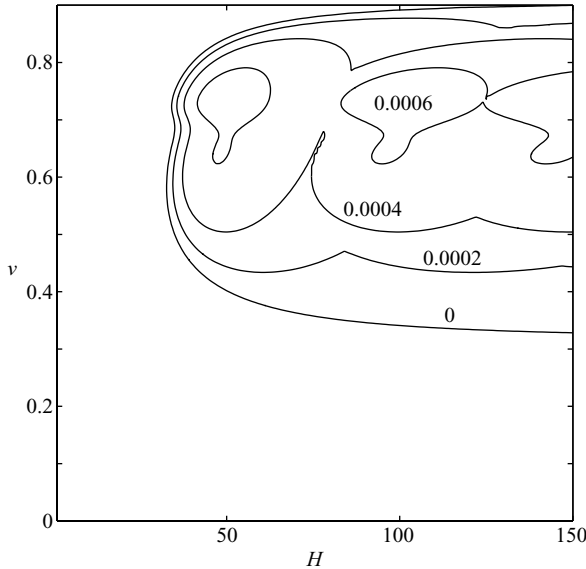


FIGURE 5. Phase diagram, showing the positive growth-rate contours, for model  $B^\kappa$  with a global equation for thermal conductivity:  $e = 0.9$ ,  $\nu_m = \pi/2\sqrt{3}$ ,  $\nu_f = 0.7$ .

4.2. Results for model B: influence of global equation of state

Figure 5 shows a phase diagram in the  $(H, \nu)$ -plane for model  $B^\kappa$ ; the flow is unstable inside the neutral contour and stable outside. Recall that this model is the same as model A for  $\nu < \nu_f$ , with the only difference being that we use a global equation for thermal conductivity which is valid upto the maximum packing density (equation (2.21)). This instability is stationary and the other features of stability diagrams remain the same (as those in figure 1 for the standard model A), but there is a dip on the neutral contour at the freezing density  $\nu = \nu_f$ . For its dense counterpart, the model  $B_d^\kappa$  does not predict any instability at large densities, but has travelling-wave

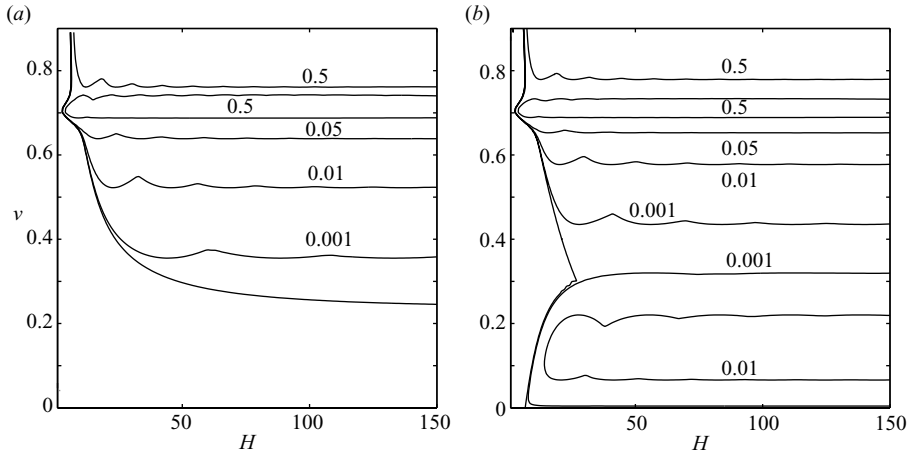


FIGURE 6. Phase diagram, showing the positive growth-rate contours, for model  $B^p$  with a global equation for pressure:  $e = 0.9$ ,  $v_m = \pi/2\sqrt{3}$ ,  $v_f = 0.7$ . (a) Full model; (b) dense limit.

instability at low densities (the corresponding stability diagram looks similar to that in figure 3(a) for model  $A_d$  and hence is not shown).

When a global equation of state for pressure is incorporated (i.e. model- $B^p$ , see §2.2), the phase diagram in the  $(H, \nu)$ -plane looks markedly different, especially at  $\nu > v_f$ , as seen in figure 6. (Recall that model  $B^p$  is same as model  $A$ , except that we use a global equation of state for pressure, equation (2.17).) In figure 6(b), the neutral stability contour contains a kink at  $\nu \approx 0.3$  and there are two instability lobes: the lower instability lobe is due to travelling waves and the upper-one is due to stationary waves. (Similar to model  $A_d$ , the low-density  $TW$  instability in figure 6(b) is dubbed ‘anomalous’ since model  $B_d$  is not valid at low densities.) For the dense limit of model  $B^p$  (i.e. model  $B_d^p$ ), the flow remains unstable to the ‘stationary’ shear-banding instability upto the maximum packing density (figure 6b). This observation is in contrast to the predictions of model  $A_d$  (figure 3a) and model  $B_d^c$ . Therefore, we conclude that within the framework of a dense model, the global equation of state for pressure induces shear-banding instabilities at large densities.

When both the global equations for pressure and thermal conductivity are incorporated, the phase diagrams in the  $(H, \nu)$ -plane look qualitatively similar (not shown) to those for model  $B^p$  as in figure 6, with the only difference being slightly higher growth rates for the least stable mode. It is noteworthy that with the global EOS, the flow becomes unstable to shear-banding instabilities at very small values of  $H$  for  $\nu \geq v_f$ .

From this section, we can conclude that within the framework of a ‘dense’ constitutive model (that incorporates only collisional contributions to transport coefficients, §2.1.2), a simple modification with a global equation of state for pressure induces new shear-banding instabilities at large densities; however, a similar modification with a global equation of state for thermal conductivity does not induce any new instability.

#### 4.3. Results for models C and D: influence of viscosity divergence

As discussed in §2.3, model C is the same as model A, with the viscosity divergence being at a lower density  $\nu = \nu_\mu < v_m$ . On the other hand, model D is the most general model that incorporates the viscosity divergence at a lower density  $\nu = \nu_\mu < v_m$

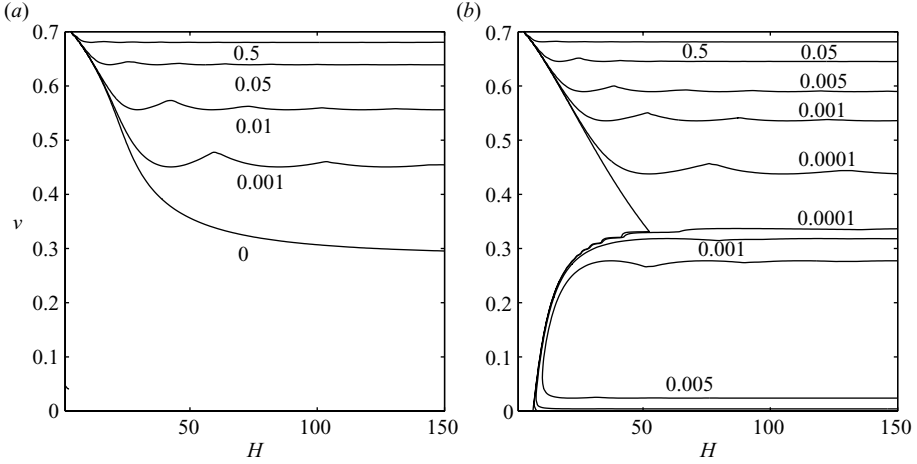


FIGURE 7. Phase diagram for model  $C$  with viscosity divergence:  $e = 0.9$ ,  $\nu_m = \pi/2\sqrt{3}$ ,  $\nu_\mu = 0.71$ . (a) Full model; (b) dense limit.

(equation (2.23)) as well as global equations for pressure (equation (2.17)) and thermal conductivity (equation (2.21)). The stability results for these two models are found to be similar, and hence we present results only for model  $C$ .

Figures 7(a) and 7(b) show phase diagrams in the  $(H, \nu)$ -plane for model  $C$  and its dense variant model  $C_d$ , respectively; the results are shown upto the viscosity divergence since uniform shear is not a solution for  $\nu > \nu_\mu$ . For the full model in figure 7(a), the phase-diagram looks similar to those for models  $A$  and  $B$ . For its dense counterpart in figure 7(b), the phase diagram is similar to that for models  $B_d$  and  $B_d^p$  in the sense that all three models support shear-banding instabilities at large densities. Therefore, for model  $C_d$ , the viscosity divergence induces shear-banding instabilities at large densities. This prediction is in tune with the results of Khain & Meerson (2006) whose model is similar to our model  $C_d$  (see § 5.3).

Within the framework of a ‘dense’ model (§ 2.1.2), therefore, we can conclude about the emergence of shear-banding instabilities at large densities that; (i) a global equation of state for pressure alone can induce shear-banding instabilities; (ii) a viscosity divergence at a density,  $\nu = \nu_\mu$ , lower than the maximum packing density alone can induce shear-banding instabilities.

### 5. Discussion: universality of shear-banding instability and crystallization

#### 5.1. An universal criterion for shear-banding instability

Since the shear-banding instability is a stationary ( $\omega_i = 0$ ) mode, this instability is given by one of the real roots (equation (3.10)) of the dispersion relation. The condition for neutral stability ( $\omega_r = 0$ ) can be obtained by setting  $\omega = 0$  in the dispersion relation (3.8):

$$a_0 = 0 \quad \Rightarrow \quad k_n^2/H^2 = \frac{\Psi_2}{\Psi_1}, \tag{5.1}$$

where

$$\Psi_1 = \frac{f_4}{f_5}, \quad \Psi_2 = \left( \frac{f_{5v}}{f_5} + \frac{f_{2v}}{f_2} \right) \frac{f_1}{f_{1v}} - 2.$$

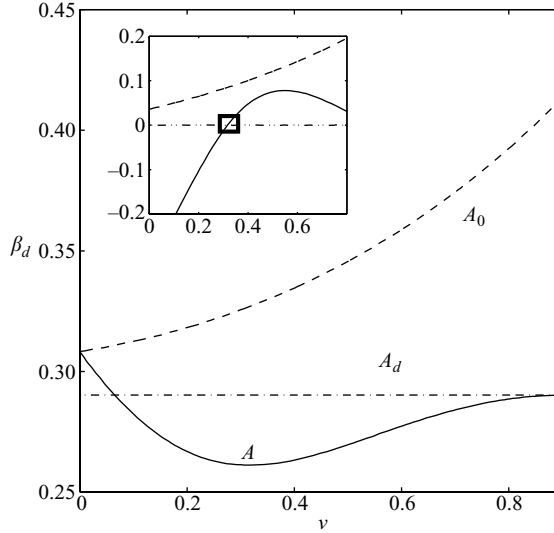


FIGURE 8. Variation of the ‘dynamic’ friction coefficient,  $\beta_d = \mu\gamma/p$ , with density for model A:  $e = 0.9$ ,  $v_m = \pi/2\sqrt{3}$ . The inset shows the variation of  $d\beta_d/d\nu$  with  $\nu$ : the onset of shear-banding instability corresponds to  $d\beta_d/d\nu > 0$ , denoted by the square.

For an instability to occur at a given density, there must be a range of ‘positive’ discrete wave-numbers, i.e.  $k_n/H > 0$ , which is equivalent to

$$\Psi_2 > 0,$$

since  $\Psi_1$  is always positive. The expression for  $\Psi_2$  can be rearranged to yield (Alam 2006)

$$\frac{d}{d\nu} \left( \frac{\sqrt{f_2 f_5}}{f_1} \right) > 0 \quad (\text{with } f_{1\nu} > 0), \quad (5.2)$$

which must be satisfied for the onset of instability. (It should be noted that (5.2) provides a necessary condition for instability, but the sufficient condition is tied to the thermal-diffusive mechanism that leads to an instability length scale (5.1) which is discussed in §5.2.) The term within the brackets in (5.2) is the ratio between the shear stress,  $P_{xy} = \mu\gamma$ , and the pressure,  $p$ , for the plane Couette flow:

$$\beta_d = \frac{P_{xy}}{p} = \frac{\mu(du/dy)}{p} = \frac{f_2\sqrt{T}}{f_1 T} = \frac{f_2}{f_1\sqrt{T}} = \frac{f_2}{f_1\sqrt{f_2/f_5}} \equiv \frac{\sqrt{f_2 f_5}}{f_1}, \quad (5.3)$$

where  $\gamma = du/dy$  is the local shear rate (which is a constant for uniform shear flow). This is merely the dynamic friction coefficient of the shear flow, which must increase with increasing density for the shear-banding instability to occur. Note that as per the Navier–Stokes-level description, the steady fully developed plane Couette flow admits solutions for which the shear stress and pressure are constants across the Couette gap. Hence, the dynamic friction coefficient,  $\beta_d = \mu(du/dy)/p = \mu\gamma/p$ , is a position-independent order-parameter for both ‘uniform’ ( $\gamma = \text{const.}$ ) and ‘non-uniform’ ( $\gamma = \gamma(y)$ ) shear flows.

For model A, the variation of  $\beta_d$  with  $\nu$  is non monotonic, as shown by the solid line in figure 8: in the dilute limit,  $\beta_d$  is large and its value decreases with increasing density until a critical density  $\nu = \nu_{cr}$  is reached beyond which  $\beta_d$  increases. Recall

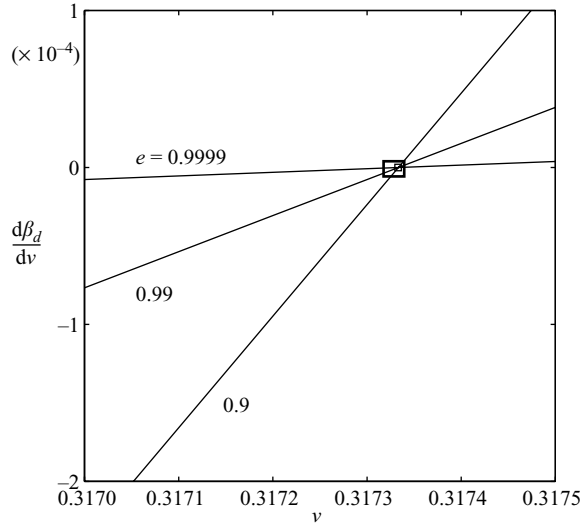


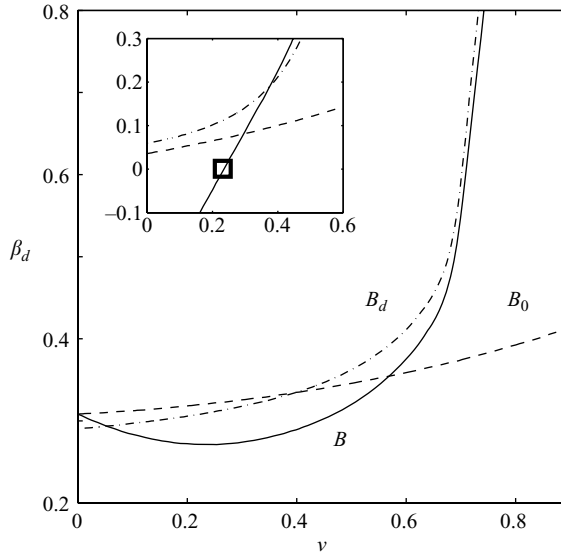
FIGURE 9. The effect of restitution coefficient  $e$  on the variation of  $d\beta_d/d\nu$  with  $\nu$  for model  $A$ .

that the onset of shear-banding instability corresponds to  $d\beta_d/d\nu > 0$ , denoted by the square in the inset of figure 8. It is clear from this inset that the full model is unstable to shear-banding instability for  $\nu > \nu_{cr}$ , the dilute model is unstable at any density (since  $d\beta_d/d\nu > 0$  for  $\nu > 0$ ), but the dense model is stable for all densities (since  $d\beta_d/d\nu = 0$ ). It is worth pointing out that, for the full model  $A$ , the critical density for the onset of the shear-banding instability (cf. figure 1) is  $\nu_{cr} \approx 0.31733$  which is independent of the restitution coefficient  $e$  as confirmed in figure 9. The lower branch of the neutral contour of figure 1 asymptotically approaches this critical density as  $H \rightarrow \infty$ .

For model  $B$ , the variation of  $\beta_d$  with density ( $\nu$ ) is shown in figure 10, and the inset shows the variation of  $d\beta_d/d\nu$  with  $\nu$ . (Recall that this model incorporates the global equations of state for pressure and thermal conductivity.) In contrast to the ‘stable’ model  $A_d$ , model  $B_d$  (i.e. the dense variant of model  $B$ ) is unstable to shear-banding instabilities for all densities (figure 6*b*) since  $d\beta_d/d\nu > 0$ . For the full model  $B$ , the critical density for the onset of shear-banding instability (cf. figure 6*a*) is  $\nu_{cr} \approx 0.2351$  which is also independent of the restitution coefficient  $e$  (as in figure 9 for model  $A$ ). For models  $C$  and  $D$ , this critical density is  $\nu_{cr} \approx 0.2849$  and  $\nu_{cr} \approx 0.2207$ , respectively.

It should be noted that there is a constraint ( $f_{1\nu} > 0$ ) with our instability criterion (5.2), i.e.  $f_1$  should be a monotonically increasing function of density for the instability to occur. This constraint on  $f_1$ , see (2.7) and (2.19), is satisfied for all four models. The consequence of a possible non-monotonic  $f_1$  is that the shear flow remains stable over a small density range between freezing and melting. However, the increasing dynamic friction with increasing density (5.2) still remains the criterion for the onset of the shear-banding instability. Even though for an unsheared elastic system,  $f_1$  is non-monotonic (Luding 2001) between freezing and melting density, we retain (2.19)–(2.20) for  $f_1$  since this functional form has been shown to hold up to the random close-packing density in simulations of plane shear flow of inelastic hard disks (Volfson *et al.* 2003).




 FIGURE 10. Same as figure 8, but for model  $B$ .

### 5.1.1. Shear-banding state and crystallization

For all four models ( $A$ ,  $B$ ,  $C$  and  $D$ ), the shear flow is stable and the system remains homogeneous at low densities, but becomes unstable to shear-banding instability beyond a critical density ( $\nu > \nu_{cr}$ ). This is because for  $\nu > \nu_{cr}$ , the flow cannot sustain the increasing dynamic friction ( $\beta_d$ ) and hence breaks into alternating layers of dilute and dense regions along the gradient direction. For  $\nu > \nu_{cr}$ , the associated ‘finite-amplitude’ bifurcated solution corresponds to a lower shear stress, or, equivalently, a lower dynamic friction coefficient. This has been verified (Alam 2008) numerically by tracking the bifurcated solutions of the associated steady nonlinear equations.

A representative set of such nonlinear bifurcated solutions for the profiles of density  $\nu(y)$ , granular temperature  $T(y)$  and streamwise velocity  $u(y)$  are displayed in figure 11 for three values of the Couette gap  $H = 50, 75$  and  $125$  for model  $A$ ; the related numerical procedure is the same as described in Alam *et al.* (2005). For this plot, the mean density is set to  $0.5$  and the restitution coefficient is  $0.9$ ; the corresponding growth-rate variation of the least stable mode can be ascertained from figure 2(a). These nonlinear solutions bifurcate from the  $n = 1$  mode (see, (3.5) and (3.6)) of the corresponding linear stability equations, and there is a pair of nonlinear solutions for each  $H$  owing to the symmetry of the plane Couette flow (Alam & Nott 1998). For mode  $n = 1$ , the density is a maximum at either of the two walls, and this density maximum approaches the maximum packing density ( $\nu_m \approx 0.906$ ) at  $H = 125$  (solid line in figure 11a) for which we have the coexistence of a ‘crystalline’ zone and a dilute zone, representing a state of phase separation. Within the crystalline zone, the granular temperature approaches zero (figure 11b) and so does the shear rate (figure 11c). It is noteworthy that the shear rate is almost uniform and localized within the dilute zone. The resulting two-phase solution is called a ‘shear-band’ (or, shear-localization) since the shearing is confined within a band of an agitated dilute region that coexists with a denser region with negligible shearing (i.e. a crystalline region at large enough Couette gap).

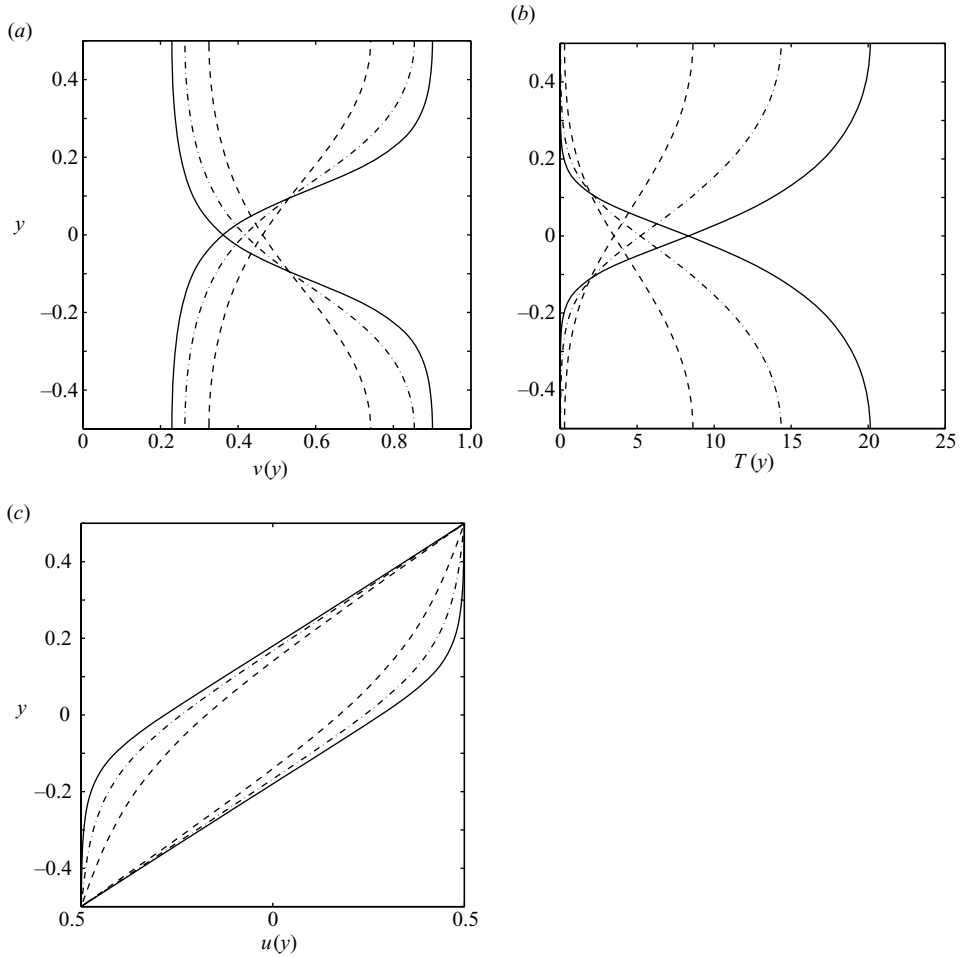


FIGURE 11. Nonlinear shear-banding solutions for model A for mode  $n=1$  with  $\nu=0.5$  and  $e=0.9$ : (a) density, (b) granular temperature and (c) streamwise velocity. ---,  $H=50$ ; -·-, 100; —, 125.

At  $H=50$  with parameters as in figure 11, there are two possible solutions: a ‘uniform-shear’ state, with the ‘dynamic’ friction coefficient being  $\beta_d \approx 0.26965$ , which is unstable, and one of two ‘shear-band’ solutions for which  $\beta_d \approx 0.2672$ . The selection of the stable branch is determined by the value of the dynamic friction coefficient being the lowest among all possible solutions, and therefore the equilibrium state of the flow (at  $H=50$ ) corresponds to the shear-banding state of a ‘lower’ dynamic friction (Alam 2008).

For higher-order modes ( $n=2, 3, \dots$ ), the shape of the nonlinear density/temperature/velocity profiles can be ascertained from (3.5) and (3.6). For example, the density profiles for modes  $n=2$  and 3 would look like the corresponding density eigenfunctions in figure 2(b). In fact, the solution for the first mode ( $n=1$ ) serves as a ‘building block’ of solutions for higher modes which has been clarified previously (Alam & Nott 1998; Nott *et al.* 1999; Alam *et al.* 2005).

At this point, we can say that an accurate constitutive model over the whole range of densities (that incorporates both kinetic and collisional modes of transport mechanisms) should be used since the dilute and dense regimes can coexist even at a moderately low mean density. Details of such shear-banding solutions for other models (*B*, *C* and *D*) and their stability as well as the related results from particle-dynamics simulations will be considered in a separate paper. Such an exercise will help to identify and tune the best among the four models.

### 5.2. Instability length scale and the effect of dissipation

While our instability criterion, given by (5.2), yields a critical value for the density above which the uniform shear flow is unstable to the shear-banding instability, it does not say anything about the related instability length scale below which the flow is stable (cf. figures 1–7). This issue of a dominant instability length scale is tied to the underlying diffusive mechanisms in a granular fluid, offered by the pseudo-thermal conductivity in the energy balance equation (2.3).

We have mentioned in §4 that the neutral contour in the  $(H, \nu)$ -plane (such as in figures 1–7) shifts towards the right with increasing restitution coefficient ( $e$ ), and hence the flow becomes more stable in the elastic limit. In fact, the dependence of the neutral contour on  $e$  can be removed if we define a normalized Couette gap as

$$H^* = H\sqrt{1 - e^2}, \quad (5.4)$$

which can be thought of as an ‘instability length scale’ (Tan & Goldhirsch 1997; Alam & Nott 1998). This length scale appears directly from an analysis of the equation for the neutral contour (5.1):

$$\begin{aligned} H^2/\Psi_1 &= k_n^2/\Psi_2 = f_3 H^2/f_4 = f_{50}(1 - e^2)H^2/f_4 \\ \Rightarrow H\sqrt{1 - e^2} &\equiv H^* = k_n \sqrt{\frac{f_4(\nu)}{\Psi_2(\nu)f_{50}(\nu)}}, \end{aligned} \quad (5.5)$$

where  $f_5(\nu, e) = (1 - e^2)f_{50}(\nu)$ , and  $f_4(\nu)$  is related to pseudo-thermal conductivity as in (2.6). This specific functional dependence of the ‘instability length scale’ on the restitution coefficient is also due to the dependence of the thermal conductivity on the granular temperature which implicitly depends on  $e$  (equation (3.2)):  $T \sim f_2/f_5 \sim (1 - e^2)^{-1}$ .

In terms of the above instability length scale (5.4), the renormalized stability diagrams in the  $(H^*, \nu)$ -plane are displayed in figure 12(a–c) for models *A–D*. In each panel, we have superimposed three neutral contours for  $e=0.9$ , 0.99 and 0.999 which are indistinguishable from each other owing to the underlying scaling (5.5) with  $e$ . In figure 12(b), we compared the neutral contour of the full model *B* with those for model *B<sup>p</sup>* (which incorporates the EOS for pressure) and model *B<sup>k</sup>* (which incorporates the global EOS for thermal conductivity). A global equation for thermal conductivity has little influence on the stability diagram, but a global equation for pressure significantly enlarges the domain of instability in the  $(H^*, \nu)$ -plane.

Comparing figures 12(a) and 12(b), we find that there is a significant difference between the predictions of models *A* and *B*, especially in the dense limit. In particular, with accurate equations of state as in model *B*, the dense flow is unstable to shear-banding instability, even for small values of the Couette gap.

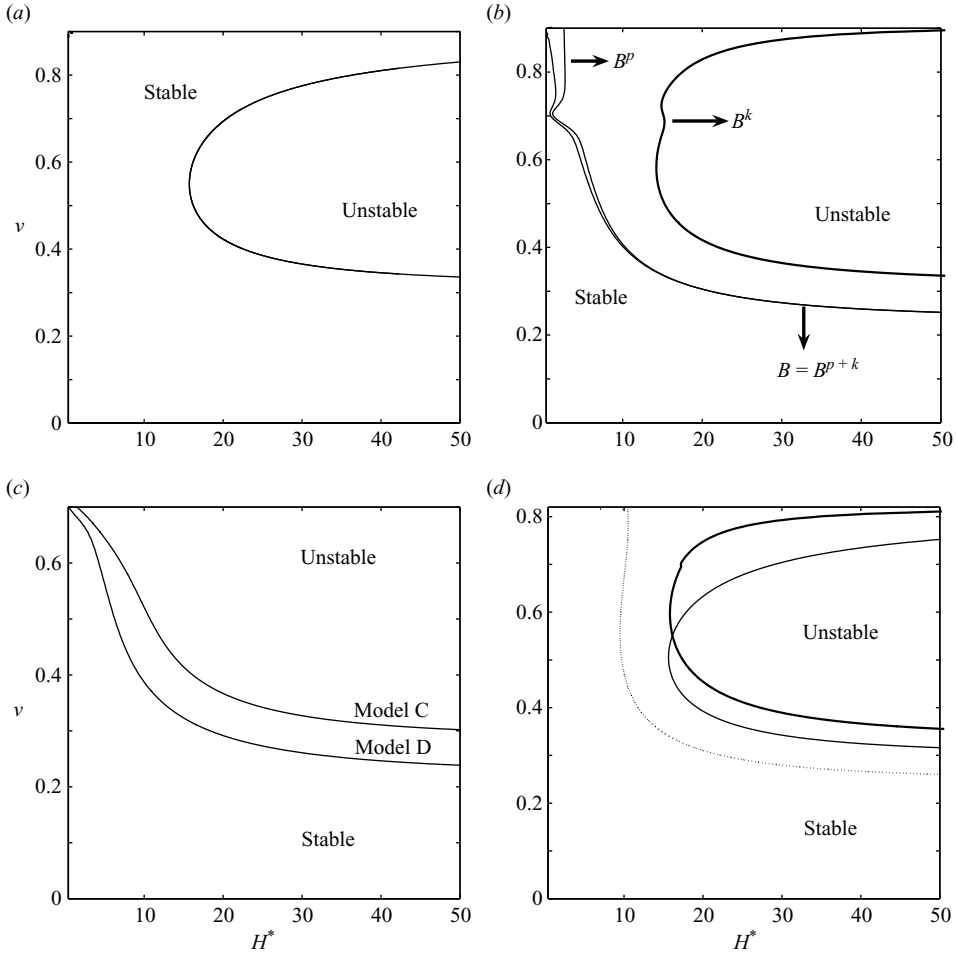


FIGURE 12. Renormalized stability diagrams in the  $(H^*, \nu)$ -plane, showing the neutral contour that separates stable and unstable regions: (a) model A; (b) model B; (c) model C and D; (d) model A with different  $\chi(\nu)$  as explained at the end of §5.2. The outermost dotted curve in (d) is discussed at the end of §5.3. In each panel, the abscissa has been renormalized as  $H^* = H\sqrt{1 - e^2}$ . Note the different range of the vertical axis in each panel.

This is an important issue beyond the square packing density  $\nu > \pi/4$  (in two dimensions) for which the flow must reorganize internally such that a part of the flow forms a layered crystalline structure or banding (Alam & Luding 2003b), thereby allowing the material to shear. This reconciles well with the predictions of model B, but not with model A (which uses the standard Enskog expressions for all transport coefficients, §2.1) for  $H^* < 30$  (figure 12a); therefore, using an accurate equation of state over the whole range of densities should give reasonable predictions for shear-banding solutions.

In this regard, the predictions of model C (upper curve in figure 12c) and model D (lower curve in figure 12c) are also consistent for dense flows since the shear-banding instabilities persist at small values of  $H$  for these models too. It may be recalled that these two models (C and D), with viscosity divergence at  $\nu = \nu_\mu < \nu_m$ , do not admit ‘uniform’ shear solution at large densities  $\nu > \nu_\mu$ . However, the related shear-banding

solutions at  $\nu < \nu_\mu$  can be continued to higher densities  $\nu > \nu_\mu$  by embedding the present problem into the uniform shear case such that the shear work is vanishingly small (Khain & Meerson 2006).

Following one referee's suggestion, we briefly discuss possible effects of Torquato's (1995) formula for the contact radial distribution function:

$$\begin{aligned} \chi(\nu) &= \frac{(1 - 0.436\nu)}{(1 - \nu)^2} \quad \text{for } 0 \leq \nu \leq \nu_f, \\ &= \frac{(1 - 0.436\nu)}{(1 - \nu_f)^2} \frac{(1 - \nu_f/\nu_r)}{(1 - \nu/\nu_r)} \quad \text{for } \nu_f \leq \nu \leq \nu_r, \end{aligned} \quad (5.6)$$

which is known to be valid for an elastic hard-disk fluid over a range of densities up to the random packing limit  $\nu_r = 0.82$ . When (5.6) is used instead of (2.12) in model A, the neutral stability curve in the  $(H^*, \nu)$ -plane follows the thick line in figure 12(d). For the sake of comparison, we have also superimposed the neutral stability curve of model A, denoted by the thin line, with  $\chi(\nu)$  being given by (2.12) with  $\nu_m = \nu_r$ . Clearly, a larger range in the dense regime is unstable with Torquato's formula (5.6), but the overall instability characteristics (the stationary nature of instability, the magnitude of growth rate, etc.) remain similar for both (2.12) and (5.6). We have also verified that the stability diagram looks similar to that in figure 5 (except for the presence of a discontinuity on the neutral contour at  $\nu = \nu_f$ , resulting in two instability lobes) when (2.20) is used as an effective contact radial distribution function for all transport coefficients.

### 5.3. Discussion of some 'ultra-dense' constitutive models

Focussing on the 'ultra-dense' regime with volume fractions close to the close-packing density ( $\nu \rightarrow \nu_m$ ), the dense limit of model A (i.e. model  $A_d$  in § 2.1.2) can be simplified by replacing  $\nu$  with  $\nu_m$  and retaining the dependence of the  $f_i$  terms on  $\nu$  via the corresponding dependence of the pair correlation function. For this ultra-dense regime the constitutive expressions are:

$$\left. \begin{aligned} f_1 &\equiv f_1^c(\nu \rightarrow \nu_m) = 2\nu_m^2 \chi, \\ f_2 &\equiv f_2^c(\nu \rightarrow \nu_m) = \frac{\sqrt{\pi}}{8} \left(1 + \frac{8}{\pi}\right) \nu_m^2 \chi, \\ f_3 &\equiv f_3^c(\nu \rightarrow \nu_m) = \frac{2}{\sqrt{\pi}} \nu_m^2 \chi, \\ f_4 &\equiv f_4^c(\nu \rightarrow \nu_m) = \sqrt{\pi} \left(\frac{1}{\pi} + \frac{9}{8}\right) \nu_m^2 \chi, \\ f_5 &\equiv f_5(\nu \rightarrow \nu_m) = \frac{4}{\sqrt{\pi}} (1 - e^2) \nu_m^2 \chi. \end{aligned} \right\} \quad (5.7)$$

This model is devoid of shear-banding instabilities since it can be verified that

$$\frac{d\beta_d}{d\nu} = 0, \quad \forall \quad \nu > 0.$$

This is similar to the predictions of model  $A_d$  (see the dot-dashed line in figure 8).

The constitutive model of Khain & Meerson (2006) can be obtained from (5.7) by replacing the contact radial distribution function for viscosity by

$$\chi \rightarrow \chi^\mu(\nu) = \left(1 + \frac{0.037}{\nu_\mu - \nu}\right) \chi(\nu)$$

which diverges at  $\nu = \nu_\mu$  as in (2.23); the exact density at which viscosity diverges is not important here. Khain & Meerson found two-phase-type solutions using their model. Since viscosity diverges at a lower density (and hence ‘faster’) than other transport coefficients, it is straightforward to verify that our instability criterion,

$$\frac{d\beta_d}{d\nu} > 0, \quad \forall \quad \nu > \nu_{cr},$$

holds for this model. Khain (2007) also found two-phase-type solutions using a constitutive model (a modified model of Khain & Meerson 2006) which is similar to our model  $D$ , and the predictions of his model agree well with particle simulation results; for this modified model too, our instability criterion (5.2) holds. Therefore, the two-phase-type solutions of Khain & Meerson (2006) and Khain (2007) are directly tied to the shear-banding instabilities of Alam & Nott (1998), Alam *et al.* (2005) and Alam (2006) via the universal instability criterion (5.2). More specifically, both belong to the same class of constitutive instability (Alam 2006).

The constitutive model of Losert *et al.* (2000) can be obtained from (5.7) by using the following functional form for the contact radial distribution function

$$\chi = (1 - \nu/\nu_r)^{-1},$$

which diverges at the random close-packing limit ( $\nu_r$ ), for all transport coefficients except the shear viscosity,  $\mu$ , that has a ‘stronger’ rate of increase near  $\nu_r$ :

$$\chi \rightarrow \chi^\mu(\nu) = (1 - \nu/\nu_r)^{-7/4}.$$

This choice of viscosity satisfies our instability criterion,  $d\beta_d/d\nu > 0$ , and, therefore, the model of Losert *et al.* would yield shear-banding-type solutions which is again tied to the increase of ‘dynamic’ friction with density for the uniform shear state.

To illustrate the quantitative effect of a stronger viscosity divergence on the shear-banding instability, the neutral stability contour for model A (with a stronger viscosity divergence, see below) is shown in figure 12(d), denoted by the outermost dotted curve. For this case, the constitutive model is the same as the full model A (i.e. all transport coefficients diverge at the same density  $\nu_m$ ) but its viscosity function  $f_2(\nu)$  in (2.8) is calculated using a radial distribution function that has a stronger divergence than all other transport coefficients:

$$\chi \rightarrow \chi^\mu(\nu) = \frac{1 - 7\nu/16}{(1 - \nu/\nu_m)^q},$$

with its exponent  $q = 2.25 > 2$ . (It should be noted that this specific functional form of  $\chi^\mu$  may not be correct quantitatively at all densities, but it has simply been chosen to illustrate the possible effects of a stronger viscosity divergence on instabilities.) Comparing the dotted contour in figure 12(d) with the thin-solid contour for model A, we find that a larger range in the  $(\nu, H^*)$ -plane is unstable for the case of a stronger viscosity divergence. With further increase of  $q$ , the neutral contour shifts towards the left to cover smaller values of  $H$ , leading to an even larger instability region in the  $(\nu, H^*)$ -plane. In either case, however, the nature of the shear-banding instability remains the same and we do not find any new instability, as emphasized before.

#### 5.4. Limit of elastic hard-sphere fluid: dissipation versus effective shear rate

Naively extrapolating the instability length scale (5.5) to the elastic limit ( $e \rightarrow 1$ ) of atomistic fluids results in  $H \rightarrow \infty$  which corresponds to an infinite system for shear banding to occur in an atomistic fluid. This is in contrast to molecular dynamics

simulations of sheared ‘elastic’ hard-sphere fluid (Erpenbeck 1984) for which a shear-induced ordering phenomenon has been observed at moderate densities (much below the freezing density). Similar observations of such banding have been made in simulations for continuous potentials too (see, Evans & Morriss 1986). The key to resolving this apparent anomaly is that the elastic limit ( $e = 1$ ) is singular since the collisional dissipation vanishes. To achieve a steady state in simulations of a sheared atomistic fluid, thermostats are used to take away energy from the system that compensates the production of energy due to shear-work ( $\mathbf{P} : \nabla \mathbf{u}$ ). Otherwise the system would continually heat up, leading to an infinite temperature. Hence, the collisional dissipation in a granular fluid can be seen to play the role of a thermostat in an atomistic fluid.

Equating the dissipation term (either due to a thermostat in an elastic fluid, or due to inelastic collisions in a granular fluid) with the shear-work, we obtain a scaling relation for temperature with the shear rate and the restitution coefficient:

$$\tilde{T} \propto \frac{\gamma^2}{1-e^2} \propto \gamma^{*2}, \quad (5.8)$$

where  $\tilde{T}$  is the dimensional temperature, and

$$\gamma^* = \frac{\gamma}{\sqrt{1-e^2}} \quad (5.9)$$

defined as an ‘effective’ shear rate. For an elastic fluid, this effective shear rate,  $\gamma^*$ , is used to normalize the temperature, and hence a similar criterion (5.2) is likely to hold for the onset of shear-banding instability in an elastic fluid too. The dependence of the effective shear rate (5.9) with inelasticity suggests that the shear-banding in atomistic fluids is likely to occur at large shear rates, a prediction that agrees with Erpenbeck’s (1984) simulations. This should be checked by determining the analytical expression for the thermostat term (which might depend on the choice of the thermostat) in the energy equation.

Although the Erpenbeck’s ordering transition has been explained (Kirkpatrick & Nieuwoudt 1986; Lutsko & Dufty 1986) as an instability of the ‘unbounded’ shear flow of an elastic fluid, using Navier–Stokes-level equations with wave-vector-dependent transport coefficients (i.e. generalized hydrodynamics), Lee *et al.* (1996) have identified a long-wave instability (with perturbations along the gradient direction only) in the uniform shear flow for all densities. In particular, Lee *et al.* showed that the Navier–Stokes-level constitutive model is the ‘minimal’ model to predict the robustness of this instability. The possible connection of this instability with the present work should be investigated in the future.

#### 5.4.1. Shearbanding criterion in a molecular fluid: Loose & Hess (1989)

We close our discussion by recalling a similar instability criterion for an ‘ordering’ transition in a dense molecular fluid (Loose & Hess 1989) and its connection (Alam 2006) with our instability criterion (5.2), along with a more general criterion for shear-banding in a shear thinning/thickening fluid.

Using a non-Newtonian constitutive model, Loose & Hess (1989) have derived a criterion for the onset of shear-banding in a dense molecular fluid:

$$\left( \frac{\partial p_{yx}}{\partial \gamma} \right) \left( \frac{\partial p_{yy}}{\partial v} \right) \leq \left( \frac{\partial p_{yx}}{\partial v} \right) \left( \frac{\partial p_{yy}}{\partial \gamma} \right), \quad (5.10)$$

where  $p_{yy}$  and  $p_{yx}$  are the normal and shear stresses, respectively. Assuming the following functional dependence of  $p_{yy}$  and  $p_{yx}$  with density ( $v$ ) and shear rate ( $\gamma$ ),

$$p_{yy} = p_{yy}^0(v)f_{yy}(\gamma), \quad p_{yx} = p_{yx}^0(v)f_{yx}(\gamma), \quad (5.11)$$

the above instability criterion simplifies to

$$\left( p_{yx}^0 \frac{df_{yx}}{d\gamma} \right) \left( f_{yy} \frac{dp_{yy}^0}{dv} \right) \leq \left( f_{yx} \frac{dp_{yx}^0}{dv} \right) \left( p_{yy}^0 \frac{df_{yy}}{d\gamma} \right). \quad (5.12)$$

For a granular fluid, the shear-rate dependence of stresses follows the well-known Bagnold scaling:

$$f_{yy}(\gamma) \sim T \sim \gamma^2, \quad f_{yx}(\gamma) \sim \gamma \sqrt{T} \sim \gamma^2, \quad (5.13)$$

where we have used the relation of the granular temperature with the shear rate,  $T \sim \gamma^2$ . Substituting (5.13) into (5.12), the Loose–Hess instability criterion boils down to (Alam 2006)

$$\frac{d}{dv} \left( \frac{p_{yx}^0}{p_{yy}^0} \right) \geq 0. \quad (5.14)$$

The term within the brackets is the dynamic friction coefficient of a fluid, and hence the onset of instability is again tied to the increasing value of this dynamic friction coefficient with increasing density. This is the same as our shear-banding instability criterion (5.3). For a more general case, the shear-rate dependence of stresses can be postulated as

$$\left. \begin{aligned} f_{yy}(\gamma) &= \gamma^{2n}, \\ f_{yx}(\gamma) &= \gamma^{n+1}, \end{aligned} \right\} \quad (5.15)$$

where the index  $n$  is a measure of shear-thickening ( $n > 0$ ) or shear-thinning ( $n < 0$ ) behaviour of the fluid. With this, the shear-banding instability criterion boils down to

$$p_{yx}^0 \frac{dp_{yy}^0}{dv} \leq \left( \frac{2n}{n+1} \right) p_{yy}^0 \frac{dp_{yx}^0}{dv}. \quad (5.16)$$

## 6. Conclusion and outlook

To conclude, we showed that by just by knowing the constitutive expressions for pressure and shear viscosity, we can determine whether any Navier–Stokes-level constitutive model would lead to a shear-banding instability in granular plane Couette flow. The onset of this stationary instability is tied to the increasing value of the ‘dynamic’ friction coefficient,  $\beta_d = \mu\gamma/p$  (where  $\mu$ ,  $p$  and  $\gamma = du/dy$  are the shear viscosity, pressure and shear rate, respectively), with increasing density for  $v > v_{cr}$  (equation (5.2)): the ‘homogeneous’ shear flow breaks into alternating layers of dilute and dense regions along the gradient direction since the flow cannot accommodate the increasing friction to stay in the homogeneous state. For  $v > v_{cr}$ , the associated ‘nonlinear’ shear-band solution corresponds to a lower shear stress, or, equivalently, a lower dynamic friction coefficient (Alam 2008). In other words, the sheared granular flow evolves toward a state of ‘lower’ dynamic friction, leading to shear-induced band formation along the gradient direction. Note that the dynamic friction coefficient,  $\beta_d = \mu\gamma/p$ , is a position-independent order-parameter for both ‘uniform’ ( $\gamma = \text{const.}$ ) and ‘non-uniform’ ( $\gamma = \gamma(y)$ ) shear flows.



In the framework of a ‘dense’ constitutive model that incorporates only the collisional transport mechanism (i.e. Haff’s model, 1983), we showed that an accurate global equation of state for pressure or a viscosity divergence at a lower density (with other transport coefficients being given by respective Enskog values) can induce shear-banding instabilities, even though the original dense Enskog model is stable to such shear-banding instabilities. Since the prediction of the shear-banding instability depends crucially on the form of the constitutive relations, we must use accurate forms of constitutive expressions over the whole range of density that incorporate both kinetic and collisional transport mechanisms. The latter statement is important since the dilute and dense regimes coexist even at a low mean density when the uniform shear flow is unstable to shear-banding instability. The resulting nonlinear shear-banding solutions of all four models (*A*, *B*, *C* and *D*) and their stability, as well as the related results from particle-dynamics simulations, will be considered in a separate paper. This will help to identify the best among these four constitutive models, or will point towards new models. In this regard, it is recommended that the particle-dynamics simulations be used to find accurate expressions (valid over the whole range of density) for all transport coefficients.

We established that the two-phase-type solutions of Khain & Meerson (2006) are directly related to the shear-banding instabilities of Alam & Nott (1998), Alam *et al.* (2005) and Alam (2006) via the universal instability criterion (5.2), and both belong to the same class of constitutive instability (Alam 2006). In particular, the instabilities arising out of non-monotonicities of constitutive relations with mean fields (e.g. the coil–stretch transition is tied to the non-monotonic stress–strain curve; see, de Gennes 1974) are of constitutive origin and hence dubbed constitutive instability. The same universal criterion (5.2) also holds for the constitutive model of Losert *et al.* (2000), thereby yielding such two-phase-type solutions in their model of plane shear flow.

The onset of the ordering transition of Erpenbeck (1984) in a sheared ‘elastic’ hard-sphere fluid (which is close to our granular system) is accompanied by a decrease in viscosity and hence a lower viscous dissipation. Therefore, similar to the sheared granular fluid, the state of lower viscosity/friction is the preferred equilibrium state for a sheared atomistic fluid. Our instability criterion (5.2) seems to provide a unified description for the shear-banding phenomena for the singular case of hard-sphere fluids if we relate the collisional dissipation to a thermostat, leading to an ‘effective’ shear rate. This possible connection should be investigated further considering the constitutive instability of the underlying field equations.

The shear-banding phenomenon is ubiquitous in a variety of complex fluids under non-equilibrium conditions: wormlike micelles (Spenley, Cates & McLeish 1993), colloidal suspensions (Hoffman 1972; Ackerson & Clark 1984), model glassy material (Varnik *et al.* 2003), suspensions of rod-like viruses (Lettinga & Dhont 2004), lyotropic liquid crystals (Olmsted 2008) and numerous other systems. In the literature of non-Newtonian fluids (see, for a review, Olmsted 2008), the shear-banding phenomenon has been explained as a constitutive instability from the linear stability analysis of appropriate constitutive models (Greco & Ball 1997; Wilson & Fielding 2005). The well-known ‘Hoffman transition’ in a colloidal suspension (banding/ordering of particles along the gradient direction) above the freezing point is accompanied by a sharp decrease in viscosity and has been explained in terms of a flow instability (Hoffman 1972). Caserta, Simeone & Guido (2008) showed that the shear-induced banding in biphasic liquid–liquid systems is tied to a lower viscosity, or, equivalently, a lower viscous dissipation. For both cases, the criterion of lower viscosity is similar to

our criterion of a lower ‘dynamic’ friction for the band-state in sheared granular fluid. It appears that the shear-induced banding in many complex fluids has a common theoretical description in terms of ‘constitutive’ instability that leads to an ordered-state of a lower viscosity/friction.

M. A. acknowledges partial funding support from DRDO, Government of India (DRDO/RN/4124) and the Max Planck Partner Group of MPI-MM Bremen at JNCASR Bangalore (MPI/MA/4190, funded by Max Planck Society, Germany).

### Appendix A. Non-dimensional equations

For non-dimensionalization, we have used  $\tilde{H}$ ,  $\tilde{H}/U_w$  and  $U_w$  as the reference length, time and velocity scales, respectively. With these scalings, the top plate moves with a velocity 1/2 and the bottom plate with  $-1/2$ . Using these quantities as reference scales, the non-dimensional forms of streamwise-independent ( $\partial/\partial x(\cdot)=0$ ) balance equations for mass, momentum and granular energy are:

$$\left(\frac{\partial}{\partial t} + v\frac{\partial}{\partial y}\right)v = -v\frac{\partial v}{\partial y}, \quad (\text{A } 1)$$

$$v\left(\frac{\partial}{\partial t} + v\frac{\partial}{\partial y}\right)u = \frac{1}{H^2}\frac{\partial}{\partial y}\left(\mu\frac{\partial u}{\partial y}\right), \quad (\text{A } 2)$$

$$v\left(\frac{\partial}{\partial t} + v\frac{\partial}{\partial y}\right)v = \frac{1}{H^2}\left[-\frac{\partial p}{\partial y} + \frac{\partial}{\partial y}\left(2\mu\frac{\partial v}{\partial y} + \lambda\frac{\partial v}{\partial y}\right)\right], \quad (\text{A } 3)$$

$$v\left(\frac{\partial}{\partial t} + v\frac{\partial}{\partial y}\right)T = \frac{1}{H^2}\frac{\partial}{\partial y}\left(\kappa\frac{\partial T}{\partial y}\right) - P\frac{\partial v}{\partial y} + 2\mu\left[\left(\frac{\partial v}{\partial y}\right)^2 + \frac{1}{2}\left(\frac{\partial u}{\partial y}\right)^2 + \frac{\lambda}{2\mu}\left(\frac{\partial v}{\partial y}\right)^2\right] - \mathcal{D}. \quad (\text{A } 4)$$

Here,  $u$  and  $v$  are the velocity components in the  $x$ - and  $y$ -directions, respectively;  $H \equiv \tilde{H}/d$  is the scaled Couette gap in terms of particle diameter. The dimensionless transport coefficients are:

$$\left. \begin{aligned} p(v, T) &= f_1(v)T, & \mu(v, T) &= f_2(v)\sqrt{T}, \\ \zeta(v, T) &= f_3(v)\sqrt{T}, & \kappa(v, T) &= f_4(v)\sqrt{T}, \\ \mathcal{D}(v, T) &= f_5(v, e)T^{3/2}, & \lambda(v, T) &= \zeta - \mu. \end{aligned} \right\} \quad (\text{A } 5)$$

### Appendix B. Coefficients of dispersion relation

The coefficients,  $a_{ij}$ , in the dispersion relation (3.8) are given by

$$a_{30} = \frac{1}{v} [\mathcal{D}_T - \mu_T], \quad (\text{B } 1)$$

$$a_{32} = \frac{1}{v} [3\mu + \lambda + \kappa] k_n^2, \quad (\text{B } 2)$$

$$a_{22} = \frac{1}{v^2} [(2\mu\mu_T + p p_T + v^2 p_v) + (3\mu + \lambda)(\mathcal{D}_T - \mu_T)] k_n^2, \quad (\text{B } 3)$$

$$a_{24} = \frac{1}{v^2} [(3\mu + \lambda)\kappa + (2\mu + \lambda)\mu] k_n^4, \quad (\text{B } 4)$$

$$a_{12} = \frac{2p_T\mu}{v^2}k_n^2 + \frac{1}{v} [p_v(\mathcal{D}_T - \mu_T) - p_T(\mathcal{D}_v - \mu_v)]k_n^2, \quad (\text{B } 5)$$

$$a_{14} = \frac{\mu}{v^3} [(2\mu + \lambda)(\mathcal{D}_T + \mu_T) + pp_T]k_n^4 + \frac{1}{v} [p_v\kappa + p_v\mu]k_n^4, \quad (\text{B } 6)$$

$$a_{16} = \frac{\mu}{v^3} [(2\mu + \lambda)\kappa]k_n^6, \quad (\text{B } 7)$$

$$a_{04} = \frac{\mu}{v^2} [p_v(\mathcal{D}_T + \mu_T) - p_T(\mathcal{D}_v + \mu_v)]k_n^4, \quad (\text{B } 8)$$

$$a_{06} = \frac{\mu}{v^2} p_v\kappa k_n^6. \quad (\text{B } 9)$$

Here,  $k_n = n\pi$ ,  $n$  is the mode number (equations (3.5) and (3.6)) and the subscripts  $v$  and  $T$  to any quantity denote its partial derivative.

#### REFERENCES

- ACKERSON, B. J. & CLARK, N. A. 1984 Shear-induced partial translational ordering of a colloidal solid. *Phys. Rev. A* **30**, 906.
- ALAM, M. 2005 Universal unfolding of pitchfork bifurcations and the shear-band formation in rapid granular Couette flow. In *Trends in Applications of Mathematics to Mechanics* (ed. Y. Wang & K. Hutter), pp. 11–20. Shaker, Aachen.
- ALAM, M. 2006 Streamwise structures and density patterns in rapid granular Couette flow: a linear stability analysis. *J. Fluid Mech.* **553**, 1.
- ALAM, M. 2008 Dynamics of sheared granular fluid. In *Proc. 12th Asian Congress of Fluid Mechanics, 18–21 August, Daejeon, Korea* (ed. H. J. Sung), pp. 1–6.
- ALAM, M. & LUDING, S. 2003a Rheology of bidisperse granular mixture via event-driven simulations. *J. Fluid Mech.* **476**, 69.
- ALAM, M. & LUDING, S. 2003b First normal stress difference and crystallization in a dense sheared granular fluid. *Phys. Fluids* **15**, 2298.
- ALAM, M. & LUDING, S. 2005 Energy nonequilibrium, rheology and microstructure in sheared bidisperse granular mixtures. *Phys. Fluids* **17**, 063303.
- ALAM, M. & NOTT, P. R. 1997 The influence of friction on the stability of unbounded granular shear flow. *J. Fluid Mech.* **343**, 267.
- ALAM, M. & NOTT, P. R. 1998 Stability of plane Couette flow of a granular material. *J. Fluid Mech.* **377**, 99.
- ALAM, M., ARAKERI, V., GODDARD, D., NOTT, P. & HERRMANN, H. 2005 Instability-induced ordering, universal unfolding and the role of gravity in granular Couette flow. *J. Fluid Mech.* **523**, 277.
- CAMPBELL, C. S. 1990 Rapid granular flows. *Annu. Rev. Fluid Mech.* **22**, 57.
- CASERTA, S., SIMEONE, M. & GUIDO, S. 2008 Shearbanding in biphasic liquid–liquid systems. *Phys. Rev. Lett.* **100**, 137801.
- CONWAY, S. & GLASSER, B. J. 2004 Density waves and coherent structures in granular Couette flow. *Phys. Fluids* **16**, 509.
- ERPENBECK, J. 1984 Shear viscosity of the hard sphere fluid via non-equilibrium molecular dynamics. *Phys. Rev. Lett.* **52**, 1333.
- EVANS, D. J. & MORRIS, G. P. 1986 Shear thickening and turbulence in simple fluids. *Phys. Rev. Lett.* **56**, 2172.
- GARCIA-ROJO, R., LUDING, S. & BREY, J. J. 2006 Transport coefficients for dense hard-disk systems. *Phys. Rev. E* **74**, 061305.
- GASS, D. M. 1971 Enskog theory for a rigid disk fluid. *J. Chem. Phys.* **54**, 1898.
- GAYEN, B. & ALAM, M. 2006 Algebraic and exponential instabilities in a sheared micropolar granular fluid. *J. Fluid Mech.* **567**, 195.
- GAYEN, B. & ALAM, M. 2008 Orientational correlation and velocity distributions in uniform shear flow of a dilute granular gas. *Phys. Rev. Lett.* **100**, 068002.

- DE GENNES, P. G. 1974 Coil-stretch transition of dilute flexible polymers under ultra-high gradients. *J. Chem. Phys.* **60**, 5030.
- GRECO, F. & BALL, R. C. 1997 Shear-band formation in a non-Newtonian fluid model with a constitutive instability. *J. Non-Newtonian Fluid Mech.* **69**, 195.
- GOLDHIRSCH, I. 2003 Rapid granular flows. *Annu. Rev. Fluid Mech.* **35**, 267.
- HAFF, P. K. 1983 Grain flow as a fluid-mechanical phenomenon. *J. Fluid Mech.* **134**, 401.
- HENDERSON, D. 1975 A simple equation of state for hard discs. *Mol. Phys.* **30**, 971.
- HOFFMAN, R. L. 1972 Discontinuous and dilatant viscosity behaviour in concentrated suspensions. I. Observation of a flow instability. *Trans. Soc. Rheol.* **16**, 155.
- HOPKINS, M. & LOUGE, M. Y. 1991 Inelastic microstructure in rapid granular flows of smooth disks. *Phys. Fluids A* **3**, 47.
- JENKINS, J. T. & RICHMAN, M. W. 1985 Kinetic theory for plane flows of a dense gas of identical, rough, inelastic, circular disks. *Phys. Fluids* **28**, 3485.
- KIRKPATRICK, T. R. & NIEUWOUTD, J. C. 1986 Stability analysis of a dense hard-sphere fluid subjected to large shear-induced ordering. *Phys. Rev. Lett.* **56**, 885.
- KHAIN, E. 2007 Hydrodynamics of fluid–solid coexistence in dense shear granular flow. *Phys. Rev. E* **75**, 051310.
- KHAIN, E. & MEERSON, B. 2006 Shear-induced crystallization of a dense rapid granular flow: hydrodynamics beyond the melting point. *Phys. Rev. E* **73**, 061301.
- LEE, M., DUFTY, J. W., MONTANERO, J. M., SANTOS, A. & LUTSKO, J. F. 1996 Long wavelength instability for uniform shear flow. *Phys. Rev. Lett.* **76**, 2702.
- LETTINGA, M. P. & DHONT, J. K. G. 2004 Non-equilibrium phase behaviour of rodlike viruses under shear flow. *J. Phys. Cond. Matter* **16**, S3929.
- LOOSE, W. & HESS, S. 1989 Rheology of dense model fluids via nonequilibrium molecular dynamics: shear-thinning and ordering transition. *Rheol. Acta* **28**, 101.
- LOSERT, W., BOCQUET, L., LUBENSKY, T. C. & GOLLUB, J. P. 2000 Particle dynamics in sheared granular matter. *Phys. Rev. Lett.* **85**, 1428.
- LUDING, S. 2001 Global equation of state of two-dimensional hard-sphere systems. *Phys. Rev. E* **63**, 042201.
- LUDING, S. 2002 Liquid–solid transition in bidisperse granulates. *Adv. Complex Syst.* **4**, 379.
- LUDING, S. 2008 From dilute to very dense granular media. Preprint.
- LUN, C. K. K., SAVAGE, S. B., JEFFREY, D. J. & CHEPURNIY, N. 1984 Kinetic theories for granular flow: inelastic particles in Couette flow and slightly inelastic particles in a general flow field. *J. Fluid Mech.* **140**, 223.
- LUTSKO, J. F. & DUFTY, J. W. 1986 Possible instability for shear-induced order-disorder transition. *Phys. Rev. Lett.* **57**, 2775.
- MCNAMARA, S. 1993 Hydrodynamic modes of a uniform granular medium. *Phys. Fluids A* **5**, 3056.
- MUETH, D. M., DEBREGAS, G. F., KARCZMAR, G. S., ENG, P. J., NAGEL, S. & JAEGER, H. J. 2000 Signatures of granular microstructure in dense shear flows. *Nature* **406**, 385.
- NOTT, P. R., ALAM, M., AGRAWAL, K., JACKSON, R. & SUNDARESAN, S. 1999 The effect of boundaries on the plane Couette flow of granular materials: a bifurcation analysis. *J. Fluid Mech.* **397**, 203.
- OLMSTED, P. D. 2008 Perspective on shear banding in complex fluids. *Rheol. Acta* **47**, 283.
- SAITOH, K. & HAYAKAWA, H. 2007 Rheology of a granular gas under a plane shear. *Phys. Rev. E* **75**, 021302.
- SAVAGE, S. B. & SAYED, S. 1984 Stresses developed by dry cohesionless granular materials sheared in an annular shear cell. *J. Fluid Mech.* **142**, 391.
- SELA, N. & GOLDHIRSCH, I. 1998 Hydrodynamic equations for rapid shear flows of smooth inelastic spheres, to Burnett order. *J. Fluid Mech.* **361**, 41.
- SHUKLA, P. & ALAM, M. 2008 Nonlinear stability of granular shear flow: Landau equation, shearbanding and universality. In *Proc. Intl Conf. on Theoretical and Applied Mechanics, 24–29 August, Adelaide, Australia*. ISBN 978-0-9805142-0-9.
- SPENLEY, N. A., CATES, M. E. & MCLEISH, T. C. B. 1993 Nonlinear rheology of wormlike micelles. *Phys. Rev. Lett.* **71**, 939.
- TAN, M. & GOLDHIRSCH, I. 1997 Intercluster interactions in rapid granular shear flows. *Phys. Fluids* **9**, 856.

- TORQUATO, S. 1995 Nearest-neighbour statistics for packings of hard spheres and disks. *Phys. Rev. E* **51**, 3170.
- TSAI, J. C., VOTH, G. A. & GOLLUB, J. P. 2003 Internal granular dynamics, shear-induced crystallization, and compaction steps. *Phys. Rev. Lett.* **91**, 064301.
- VARNIK, F., BOCQUET, L., BARRAT, J.-L. & BERTHIER, L. 2003 Shear localization in model glass. *Phys. Rev. Lett.* **90**, 095702.
- VOLFSON, D., TSIMRING, L. S. & ARANSON, I. S. 2003 Partially fluidized shear granular flows: continuum theory and molecular dynamics simulations. *Phys. Rev. E* **68**, 021301.
- WILSON, H. J. & FIELDING, S. M. 2005 Linear instability of planer shear banded flow of both diffusive and non-diffusive Johnson–Segelman fluids. *J. Non-Newtonian Fluid Mech.* **138**, 181.